Optics Letters

Laser fabrication of graphene-based electrothermal actuators enabling predicable deformation

Lin Zhu,[1] Yuan-Yuan Gao,[1] Bing Han,[1] Yong-Lai Zhang,[1,*] and Hong-Bo Sun[1,2]

[1]State Key Laboratory of Integrated Optoelectronics, College of Electronic Science and Engineering, Jilin University, 2699 Qianjin Street, Changchun 130012, China
[2]State Key Laboratory of Precision Measurement Technology & Instruments, Department of Precision Instrument, Tsinghua University, Haidian district, Beijing 100084, China
*Corresponding author: yonglaizhang@jlu.edu.cn

Received 13 December 2018; revised 23 January 2019; accepted 7 February 2019; posted 11 February 2019 (Doc. ID 355166); published 7 March 2019

Electrothermal actuators (ETAs) that can convert electric energy into mechanical works have been extensively studied for their great potential in artificial muscles and robotics. However, the production of ETAs that enable complex and predictable deformation is still challenging. In this Letter, an ETA based on reduced graphene oxide (RGO) and polyethylene (PE) bimorph is developed through a facile laser-scribing method. Since the laser-scribing technology permits flexible patterning, conductive RGO electrodes with complex circuit patterns can be readily produced on a thermally active PE film, forming an ETA capable of fast and reversible deformation. In addition, the laser-scribed ETA demonstrated orientation-defined bending performance, enabling more sophisticated deformation control. The laser scribing of graphene oxide has opened up a new way to produce ETAs towards cutting-edge applications such as soft robotics and intelligent systems.

https://doi.org/10.1364/OL.44.001363

Actuators that can convert external stimuli to mechanical motions have attracted great research interest in the fields of soft robotics, artificial muscles, micro-electromechanical systems, and various automatic systems [1–4]. To date, various stimuli responsive actuators that can be manipulated by light [5], chemicals [6], moisture [7–9], electricity [10,11], and heat [12] have been successfully developed through different energy conversion mechanisms. For example, Cheng *et al.* successfully fabricated the moisture responsive graphene fibers by selective laser modification [9]; Wang *et al.* reported the superhydrophobic and photothermal gear that can be actuated by the Marangoni effect [4]; Han *et al.* developed a plasma-assisted light-driven bimorph actuator that consists of a layer of gold nanorods loaded graphene oxide (GO) and a layer of polymethyl methacrylate, revealing great potential for bionic robots and artificial muscles [5].

Among the above-mentioned actuators, electrical actuators are distinguished due to their high controllability and flexibility for manipulation [13–20]. Generally, electrical actuators can be divided into three categories: (1) electronic actuators that respond to electric charge [13,14], (2) ionic actuators driven by ion migration [15–17], and (3) electrothermal actuators (ETAs) that resort to an electrothermal effect [18–20]. Since two former kinds of actuators have their own limitations of high driving voltage and indispensable electrolyte environment, the ETAs have emerged as an appealing alternative for their distinct merits of low driving voltage, electrolyte-free, lightweight, and easy operation.

ETAs are generally based on bilayers that have distinct coefficients of thermal expansion (CTEs), in which one layer is electrothermally active, and the other layer enables thermal expansion [18–20]. Under electric actuation, the electrothermal layer can convert the electric energy into joule heat, leading to an increase of local temperature. Due to the distinct CTEs of the bilayers, an obvious mismatch of strain at the bilayer interface is generated and, thus, the bilayer bends to the side with smaller CTE value. According to this basic design principle, ETAs that feature fast and reversible deformation have been successfully produced using different materials. In spite of the rapid advancements, there still exist several open problems that should be addressed urgently. For instance, carbon nanomaterials such as carbon nanotube and graphene have been widely employed as an electrothermally layer considering their advantages of excellent conductivity, negative CTEs, high thermal conductivity, chemical stability, and outstanding mechanical performance [21–28]. However, the fabrication of conductive patterns based on these carbon materials becomes the main barrier for developing carbon-based ETAs, since the processes usually involve complex procedures or rely on special equipment [29–32]. Besides, most of the reported actuators that consist of "I-" or "U-"shaped electrothermal patterns can only accomplish very simple deformation, for instance, bending, which cannot meet the gradually increased requirement of applications in soft robotics [18,33–35]. Few works that allow different bending performance still have problems with flexible patterning and simple fabrication [18]. Currently, programmable patterning of carbon

electrothermal layers for developing ETAs that enables complex and predictable deformation is highly desirable, but it remains a big challenge.

In this Letter, we report a laser-scribing strategy for producing patterned reduced graphene oxide (RGO) electrothermal layer on a polyethylene (PE) film, enabling facile fabrication of graphene-based ETAs. Programmable laser scribing on graphene oxide (GO) films can trigger the removal of oxygen groups on GO sheets effectively, which renders its conductivity and leads to the formation of conductive electrothermal patterns with arbitrary shapes. Since GO/RGO and PE feature distinct CTEs (GO/RGO: -6×10^{-6}/K, PE: 20×10^{-5}/K), the electrothermal effect would induce an obvious strain mismatch at the bilayer interface, leading to bending deformation towards the graphene side. Besides, laser scanning-induced RGO stripes with special orientation can further govern the bending direction of the ETAs, proving the possibility for more sophisticated deformation control. As a proof of concept, a bionic flytrap robot has been demonstrated for controllably capturing and releasing objects.

The simple and fast fabrication process of the RGO/PE bilayer film is shown in Fig. 1(a). First, a GO solution prepared by a modified Hummers method is dripped directly on the PE film-coated DVD disk [36,37]. After drying GO naturally, the GO and PE-coated DVD disk is inserted into a light-scribe enabled optical drive (HP Inc. 557S) for subsequent laser-scribing process (laser source, 780 nm focused near-infrared laser; intensity, 5 mW; spot size, ~6 μm). The DVD can be located and written repeatedly by Nero StartSmart Essentials software, which ensures precisely the reduction of GO according to predesigned patterns [38–40]. The whole reducing process takes no more than 25 min for one disk, which can produce several or even dozens of circuit patterns depending on the size of the actuators. The optical photos of a laser-scribed GO film are shown in Fig. 1(b); the golden-brown GO turn into black RGO with electrical conductivity at accurate locations, and the circuits with positive and negative (–) terminals are designed to form conductive path for further actuating operation under applied voltage. After the bilayer film is peeled off from the disk and connected to the voltage source with copper wires, an electric-driven laser-scribed RGO (LsrGO)/PE actuator is obtained. Figure 1(c) is a schematic diagram that shows the details of the prepared LsrGO/PE ETA. The RGO path serves as an electrothermal layer which converts the input electric energy into joule heat according to electrothermal energy conversion; meanwhile, the PE layer is the thermal expansion layer owing to its high CTE ($15 * 10^{-5}$/K). When applied with voltage, the conductive RGO region heats up the whole structure. The PE layer expends drastically, while the LsrGO almost keeps unchanged, leading to the actuation of the LsrGO/PE bilayer film, as shown in Fig. 1(d).

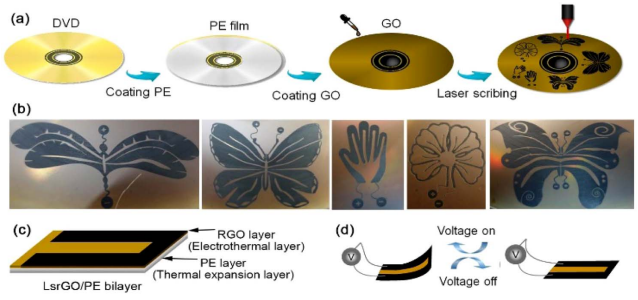

Fig. 1. (a) Schematics illustration of fabrication procedure of the LsrGO/PE bilayer film. (b) Various programmable circuit patterns for complex electro-driven actuations. (c) Schematics illustration of the electrothermal actuation mechanism of a U-shaped LsrGO/PE ETA.

To explore the reduction effect of light scribing on the GO/PE film, the X-ray photoelectron spectroscopy (XPS) analysis, the electrical testing (resistance) and the Raman spectra are carried out in room temperature (~26°C) and ambient humidity (~45%). The C1 XPS spectra of GO/PE film and LsrGO/PE film which, before and after laser scribing, are shown in Figs. 2(a) and 2(b). The C1 spectra are mainly concerned with the oxygen and carbon content of the GO. Four typical binding energy peaks of GO at 284.8, 286.9, 287.4, and 288.9 eV represents C-C (non-oxygenated ring carbon), C-O (hydroxyl and epoxy carbon groups), C = O (carbonyl groups), and O-C = O (ester groups), respectively [Fig. 2(a)]. After laser treatment, the intensities of the relative oxygen contained groups (OCGs), including C-O, C = O, and O-C = O decrease drastically, conforming the removal of OCGs, which means GO has been successfully reduced to RGO [Fig. 2(b)]. Besides, according to XPS spectrum result, the content of oxygen element after 10, 20, 30, 40 and 100 times cycling is 11.62%, 11.1%, 11.97%, 11.26%, and 11.07%, respectively, which shows the stability of the ETA for cycling usage.

The current-voltage (I–V) curves of as prepared GO/PE film before and after laser scribing is shown in Fig. 2(c). The original U-shaped GO film (355 mm^2) is insulated as the current stays 0 under test voltage from −10 to +10 V. The LsrGO is proved to be conductive, and its resistance is calculated to be 30 KΩ, according to Ohm's law ($R = V/I$). The results confirm laser scribing as an effective way to obtain conductive RGO with patterned superiority. Taking advantage of the maskless pattern property of a laser-scribing approach, various patterns with different distribution of RGO and GO can be obtained. Moreover, various deformations and complex motions can be achieved.

The Raman spectra (room temperature and ambient humidity, ~26°C, 45%) in Fig. 2(d) give a further understanding of graphitized degree of the GO/PE film and LsrGO/PE film. The two characteristic bands of graphitized carbon are observed at 1350 (D band) and 1590 cm^{-1} (G band). The D band is generated by sp3-hybridized carbon vibrations, and the G band is

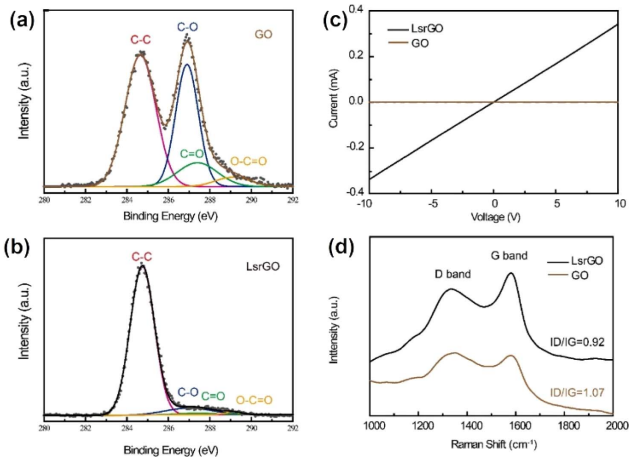

Fig. 2. C1 XPS spectra of (a) GO and (b) LsrGO. (c) Current-voltage relationships of the GO and LsrGO. (d) Raman spectra of GO and LsrGO.

attributed to the E2g phonon of C sp2 atoms. Normally, the ratio of the D peak intensity value to the G peak intensity value (I_D/I_G) is used to express the disorder degree of graphite, which is slightly decreasing after laser scribing in this case [41]. The results indicate the recovery of sp^2 carbon induced by photoreduction.

In order to verify the thickness of the thermal expansion layer (PE layer) impacting on bending performance, different U-shaped actuators [in Fig. 1(d)] with PE film thicknesses of 30, 50, and 80 μm are investigated [inset of Fig. 3(a)], expressed in LsrGO/PE (30 μm), LsrGO/PE (50 μm), and LsrGO/PE (80 μm), respectively. The bending performance is quantified by the curvature (1/R) of the actuator [inset of Fig. 3(c)]. Figure 3(a) records the maximum curvature of the actuators under different voltage (30, 35, 40, 45, 50, 55, and 60 V). The LsrGO/PE (30 μm) shows the best performance in all conditions. This is because thinner film needs less driving force to achieve its deformation. In other words, with equal joule heat generated by the same RGO channel under a certain voltage, films with a thinner PE layer tend to perform larger deformation. Hence, the LsrGO/PE (30 μm) is used for further experiment.

The temperature change of the actuator varies with different driving voltages (30, 40, 50, and 60 V) is measured by an infrared camera, as shown in Fig. 3(b). Figure 3(c) illustrates the corresponding curvature change as a function of input voltage. Initially, the temperature of the U-shaped actuator equals room temperature (about 26°C) without input voltage. Once the voltage is on, the temperature increases gradually and then reaches a stable highest value when the heat loss equals the generated heat. After the voltage is switched off, the temperature decreases to the original state. The result shows that with higher input voltage, the actuator could reach a higher temperature, which matches the Joule's law $Q = U^2t/R$. Generally, for the same U-shaped actuator, the resistance remains unchanged; however, larger driving voltage leads to higher joule heat. The bending curvature varies as the same tendency with temperature change, as shown in Fig. 3(c). The actuator bends and recovers, along with the temperature rising and falling. In detail, the bending curvature increases with the input voltage increment, that is, achieving a higher temperature, so that the expansion mismatch between the two layers becomes larger, leading to a greater extent of bending.

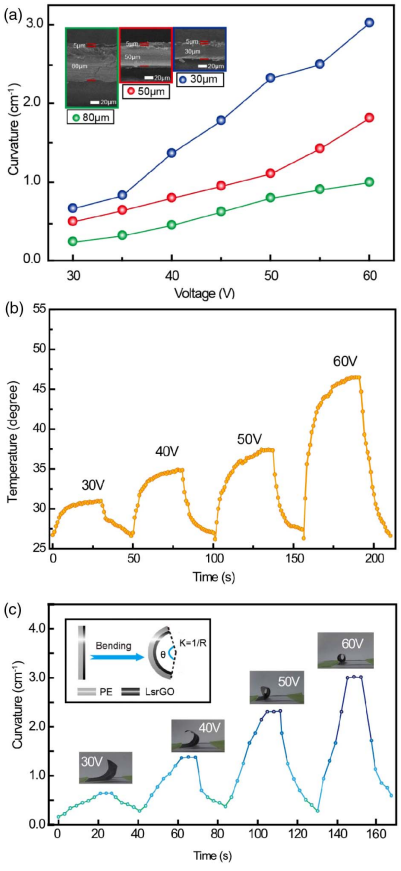

Fig. 3. (a) Maximum bending curvature under different driving voltages of ETAs with different PE thicknesses. (b) Temperature changes of the LsrGO/PE (30 μm) as a function of time under voltages from 30 to 60 V (30, 40, 50, and 60 V). (c) Time-dependent curvature variation corresponding to (b).

The morphology (room temperature and ambient humidity, ~26°C, 45%) of laser-scribed RGO film can be observed in Fig. 4(a); the GO film turns into loose exfoliated layers along with the laser scanning path [inset of Fig. 4(a)] while the untreated region remains smooth. The confocal laser scanning microscopy (CLSM) further shows the rough surface of the laser-scribing channel [Fig. 4(b)]. When applying electric power to the RGO/PE bilayer, the current flows through the laser scanning path of conductive RGO and generates joule heat. Due to the thermal expansion of the PE layer, the bimorph bends in response to the strain mismatch at the bilayer interface. Interestingly, the RGO/PE bimorph presents an oriented bending performance that is always perpendicular to the laser-scribing direction due to the anisotropic microstructures formed by the circular laser scribing. Specifically, bending perpendicularly to the grating structures [Fig. 4(a)] would suffer much smaller resistance. Inspired by this phenomenon, a cross-shaped GO/PE actuator with a different pre-design path of LsrGO is designed, as illustrated in Figs. 4(d) and 4(e). When the LsrGO path is transversely arranged [Fig. 4(d)], the actuator bends in an up and down directions. In contrast, when the LsrGO path is longitudinally designed, as shown in Fig. 4(e), the actuator bends in the left and right directions. Based on these distinct types of performances, multiform actuations can be achieved through complex pre-designed patterns and anisotropy behaviors. Figure 5 shows a complex functional ETA inspired by natural flytraps. First, a flytrap-shaped actuator

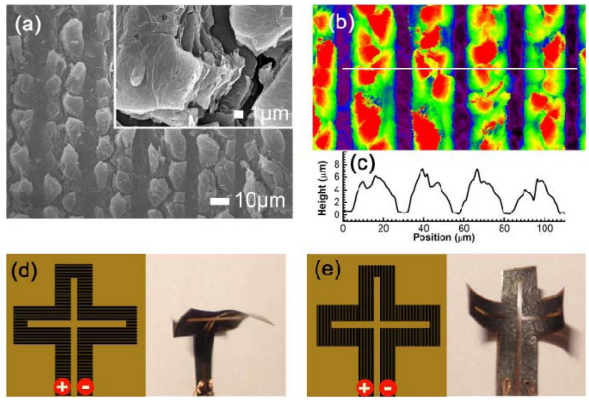

Fig. 4. (a) SEM image of exfoliated LsRGO surface. (b) CLSM image and corresponding height profiles of the LsRGO/PE film. Different bending performance of a cross-shaped ETA with (d) transversely and (e) longitudinally arranged laser-scribing paths.

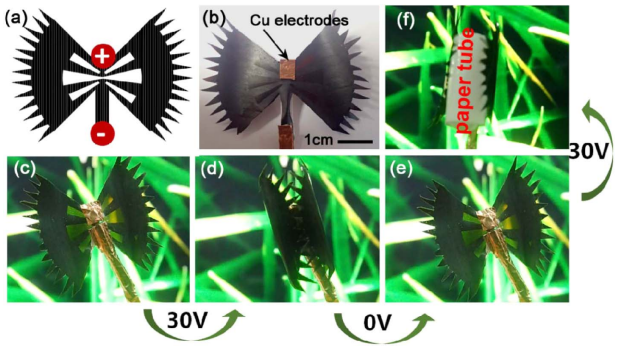

Fig. 5. Bionic flytrap robot based on the ETA. (a) Designed circuit pattern and (b) photograph of the flytrap-shaped actuator. (c)–(e) Real-time photographs of the ETA with and without driving voltage. (f) Grasping function of the ETA flytrap.

with a parallel conductive circuit is fabricated through laser scribing [Fig. 5(b)], and the design of the parallel loops leads to a smaller resistance (10 KΩ) than the former U-shaped actuator (30 KΩ), which generates a higher joule heat under the same voltage and leads to a faster response. The ETA can achieve a closing posture like a real flytrap under 30 V within 5 s and return to the open state after switching off the input power [Figs. 5(c)–5(e)]. In addition, the flytrap-shaped ETA can capture and hold a paper tube with a slippery surface [Fig. 5(f)]. This indicates the strong grasping force of the ETA.

In summary, an ETA composed of RGO and PE bimorph with programmable patterned electrothermal circuits is fabricated through a simple laser-scribing method. The resultant bimorph ETA performs fast, large-scale, and orientation-defined bending performance, processing multiform but controllable actuation ability. As a proof of concept, a flytrap-shaped ETA with actual grasping function is designed and fabricated successfully, resulting in a quick response (5 s), large deformation (1 cm^{-1}) under a human safety input voltage (30 V). The laser-scribing fabrication method reported in this Letter may open up a new way for developing ETAs with a fast response and multiform deformation, revealing great potential for flexible actuation, artificial muscles, and bionic robots.

Funding. National Key Research and Development Program of China (2017YFB1104300); National Natural Science Foundation of China (NSFC) (#61775078, #61590930, #61605055, #61522503).

REFERENCES

1. B. Han, Y. L. Zhang, Q. D. Chen, and H. B. Sun, Adv. Funct. Mater. **28**, 1802235 (2018).
2. Q. M. Chen, X. W. Yu, Z. Q. Pei, Y. Yang, Y. Wei, and Y. Ji, Chem. Sci. **8**, 724 (2017).
3. L. Hines, K. Petersen, G. Z. Lum, and M. Sitti, Adv. Mater. **29**, 1603483 (2017).
4. W. Wang, Y. Q. Liu, Y. Liu, B. Han, H. Wang, D. D. Han, J. N. Wang, Y. L. Zhang, and H. B. Sun, Adv. Funct. Mater. **27**, 1702946 (2017).
5. B. Han, Y. L. Zhang, L. Zhu, Y. Li, Z. C. Ma, Y. Q. Liu, X. L. Zhang, X. W. Cao, Q. D. Chen, C. W. Qiu, and H. B. Sun, Adv. Mater. **31**, 1806386 (2018).
6. Q. Zhao, J. W. C. Dunlop, X. L. Qiu, F. H. Huang, Z. B. Zhang, J. Heyda, J. Dzubiella, M. Antonietti, and J. Y. Yuan, Nat. Commun. **5**, 4239 (2014).
7. B. Yang, W. T. Bi, C. A. Zhong, M. C. Huang, Y. Ni, L. H. He, and C. Z. Wu, Sci. China Mater. **61**, 1291 (2018).
8. H. X. Chen, T. T. You, G. Xu, Y. K. Gao, C. M. Zhang, N. Yang, and P. G. Yin, Sci. China Mater. **61**, 1201 (2018).
9. H. H. Cheng, J. Liu, Y. Zhao, C. G. Hu, Z. P. Zhang, N. Chen, L. Jiang, and L. T. Qu, Angew. Chem. (Int. Ed.) **52**, 10482 (2013).
10. S. Taccola, F. Greco, E. Sinibaldi, A. Mondini, B. Mazzolai, and V. Mattoli, Adv. Mater. **27**, 1668 (2015).
11. P. N. Chen, S. S. He, Y. F. Xu, X. M. Sun, and H. S. Peng, Adv. Mater. **27**, 4982 (2015).
12. W. Zhang, H. Zappe, and A. Seifert, Light: Sci. Appl. **3**, e145 (2014).
13. K. B. Subramani, E. Cakmak, R. J. Spontak, and T. K. Ghosh, Adv. Mater. **26**, 2949 (2014).
14. J. H. Wu, J. F. Zang, A. R. Rathmell, X. H. Zhao, and B. J. Wiley, Nano Lett. **13**, 2381 (2013).
15. X. J. Xie, L. T. Qu, C. Zhou, Y. Li, J. Zhu, H. Bai, G. Q. Shi, and L. M. Dai, ACS Nano **4**, 6050 (2010).
16. O. Kim, T. J. Shin, and M. J. Park, Nat. Commun. **4**, 2208 (2013).
17. J. Kim, J. H. Jeon, H. J. Kim, H. Lim, and I. K. Oh, ACS Nano **8**, 2986 (2014).
18. Q. W. Li, C. H. Liu, Y. H. Lin, L. Liu, K. L. Jiang, and S. S. Fan, ACS Nano **9**, 409 (2015).
19. L. Z. Chen, M. C. Weng, Z. W. Zhou, Y. Zhou, L. L. Zhang, J. X. Li, Z. G. Huang, W. Zhang, C. H. Liu, and S. S. Fan, ACS Nano **9**, 12189 (2015).
20. Z. W. Zhou, Q. W. Li, L. Z. Chen, C. H. Liu, and S. S. Fan, J. Mater. Chem. B **4**, 1228 (2016).
21. T. W. Ebbesen, H. J. Lezec, H. Hiura, J. W. Bennett, H. F. Ghaemi, and T. Thio, Nature **382**, 54 (1996).
22. Y. A. Kim, H. Muramatsu, T. Hayashi, M. Endo, M. Terrones, and M. S. Dresselhaus, Chem. Phys. Lett. **398**, 87 (2004).
23. F. Inam, H. Yan, M. J. Reece, and T. Peijs, Adv. Appl. Ceram. **109**, 240 (2010).
24. A. K. Geim and K. S. Novoselov, Nat. Mater. **6**, 183 (2007).
25. A. A. Balandin, Nat. Mater. **10**, 569 (2011).
26. S. Ghosh, I. Calizo, D. Teweldebrhan, E. P. Pokatilov, D. L. Nika, A. A. Balandin, W. Bao, F. Miao, and C. N. Lau, Appl. Phys. Lett. **92**, 159111 (2008).
27. Q. Y. Xu, T. Ma, M. Danesh, B. N. Shivananju, S. Gan, J. C. Song, C. W. Qiu, H. M. Cheng, W. C. Ren, and Q. L. Bao, Light: Sci. Appl. **6**, e16204 (2017).
28. M. Q. Jian, C. Y. Wang, Q. Wang, H. M. Wang, K. L. Xia, Z. Yin, M. C. Zhang, X. P. Liang, and Y. Y. Zhang, Sci. China Mater. **60**, 1026 (2017).
29. L. M. Dai and A. W. H. Mau, Adv. Mater. **13**, 899 (2001).
30. L. Q. Jiang, L. Gao, and J. Sun, J. Colloid Interface Sci. **260**, 89 (2003).
31. X. S. Li, W. W. Cai, J. H. An, S. Kim, J. Nah, D. X. Yang, R. Piner, A. Velamakanni, I. Jung, E. Tutuc, S. K. Banerjee, L. Colombo, and R. S. Ruoff, Science **324**, 1312 (2009).
32. E. Dervishi, Z. R. Li, F. Watanabe, A. Biswas, Y. Xu, A. R. Biris, V. Saini, and A. S. Biris, Chem. Commun. **27**, 4061 (2009).
33. L. Z. Chen, C. H. Liu, C. H. Hu, and S. S. Fan, Appl. Phys. Lett. **92**, 339 (2008).
34. A. T. Sellinger, D. H. Wang, L. S. Tan, and R. A. Vaia, Adv. Mater. **22**, 3430 (2010).
35. Y. Hu, W. Chen, L. H. Lu, J. H. Liu, and C. R. Chang, ACS Nano **4**, 3498 (2010).
36. H. J. Shin, K. K. Kim, A. Benayad, S. M. Yoon, H. K. Park, I. S. Jung, M. H. Jin, H. K. Jeong, J. M. Kim, J. Y. Choi, and Y. H. Lee, Adv. Funct. Mater. **19**, 1987 (2009).
37. Y. W. Zhu, M. D. Stoller, W. W. Cai, A. Velamakanni, R. D. Piner, D. Chen, and R. S. Ruoff, ACS Nano **4**, 1227 (2010).
38. M. F. El-Kady, V. Strong, S. Dubin, and R. B. Kaner, Science **335**, 1326 (2012).
39. H. Tian, C. Li, M. A. Mohammad, Y. L. Cui, W. T. Mi, Y. Yang, D. Xie, and T. L. Ren, ACS Nano **8**, 5883 (2014).
40. B. Han, Y. L. Zhang, L. Zhu, X. H. Chen, Z. C. Ma, X. L. Zhang, J. N. Wang, W. Wang, Y. Q. Liu, Q. D. Chen, and H. B. Sun, Sens. Actuators, B. **270**, 500 (2018).
41. V. E. Muradyan, A. A. Arbuzov, E. A. Sokolov, S. D. Babenko, and G. V. Bondarenko, Tech. Phys. Lett. **39**, 798 (2013).